



Article

# Autonomous Installation of Electrical Spacers on Power Lines Using Magnetic Localization and Special End Effector

Filip Zorić <sup>1,\*</sup> , Stjepan Flegarić <sup>2</sup> , Goran Vasiljević <sup>1</sup> , Stjepan Bogdan <sup>1</sup> and Zdenko Kovačić <sup>1</sup> <sup>1</sup> Faculty of Electrical Engineering and Computing, University of Zagreb, 10000 Zagreb, Croatia<sup>2</sup> Faculty of the Mechanical Engineering and Naval Architecture, University of Zagreb, 10000 Zagreb, Croatia

\* Correspondence: filip.zoric@fer.hr

**Abstract:** The combined effects of environmental factors such as high winds and melting ice can cause transmission line conductors to vibrate at high amplitudes, resulting in damaged pole structures, cracked insulating strands, and short circuits. The manual installation of electrical spacers between the two power line conductors is currently the only way to prevent this, but due to the high-voltage environment, this operation is extremely dangerous for a human worker. As a solution to automate this operation, the autonomous installation of electrical spacers using a robotic manipulator is proposed. For this purpose, a design of a special end effector for the robotic installation of electrical spacers is proposed. The end effector prototype was produced and tested under laboratory conditions and then used for the autonomous installation of spacers on power lines. Its localization with respect to the power lines is based on measurements of the magnetic field generated by the alternating currents flowing through the power lines. To verify the feasibility of the proposed solution under laboratory conditions, the proposed end effector equipped with magnetometers was developed and mounted on a 6-axis Schunk LWA 4p robotic arm. The implemented autonomous installation sequence was successfully verified using a robot and a laboratory mock-up of power lines.

**Keywords:** end effector; magnetic localization; manipulation planning; service robotics; power lines

**Citation:** Zoric, F.; Flegaric, S.; Vasiljevic, G.; Bogdan, S.; Kovacic, Z. Autonomous Installation of Electrical Spacers on Power Lines Using Magnetic Localization and Special End Effector. *Machines* **2023**, *11*, 510. <https://doi.org/10.3390/machines11050510>

Academic Editors: Zheng Chen, Muhammad Hassan Tanveer, David A. Guerra-Zubiaga and Sumit Chakravarty

Received: 27 March 2023

Revised: 14 April 2023

Accepted: 19 April 2023

Published: 24 April 2023



**Copyright:** © 2023 by the authors. Licensee MDPI, Basel, Switzerland. This article is an open access article distributed under the terms and conditions of the Creative Commons Attribution (CC BY) license (<https://creativecommons.org/licenses/by/4.0/>).

## 1. Introduction

The main objective of the AERIAL-CORE (<https://aerial-core.eu/> (accessed on 16 February 2023); see Funding section for more information) project is to develop an advanced aerial robotic system for the maintenance and repair of large linear infrastructures, focusing on power lines, which are used almost everywhere as the main carrier of electrical energy between urban areas. This technical infrastructure requires regular maintenance to ensure continuous power transmission. To ensure this, potential hazards caused by environmental factors must be minimized. Environmental hazards are usually caused by wind and icing [1]. Their combined effect can sometimes cause the conductors to gallop, vibrating the transmission line conductors at a high amplitude [2]. Conductor galloping can result in damaged pole structures, cracked insulating strands, and short circuits.

The primary method of reducing such risks is to install mechanical devices referred to as electrical spacers, dampers, distancers, or interphase spacers [2]. Electrical spacers are used to prevent the most dangerous phase-to-phase short circuits. Currently, their installation poses a very high risk to operators due to the high voltage, difficult access, and high altitude [3]. Very often, the installation is done with a helicopter or an aerial bridge (crane) from which a worker hangs very close to the power lines. In addition to these life-threatening risks, human workers must take strict safety precautions and wear special clothing, which limits human dexterity and increases the operation and maintenance time that must be spent to install certain equipment on the power line, which in turn drives up long-term maintenance costs [4].

To minimize the risk to personnel performing various maintenance and repair tasks in such infrastructures, one idea is to develop advanced autonomous robotic systems that

can replace humans. Due to the physical characteristics of such systems, aerial robotic manipulators could provide an ideal solution to the above problems [5]. Due to the complexity of the tasks performed on power lines, practical robotic solutions that can handle this complexity require the combination of novel perception, manipulation, and control algorithms implemented in aerial robotic manipulator systems (Figure 1).



**Figure 1.** The concept of installing electrical spacers on power lines by an aerial manipulator.

The main objective of this paper is to analyze an electric spacer installation task, present a developed special end effector for this task, and control the motion of a robotic manipulator holding the end effector using a magnetic-field-based localization system developed for the fully autonomous installation of electric spacers on an in-phase parallel power line. Based on these objectives, the contributions of this paper are:

1. The mechanical design of an end effector for the autonomous installation of spacers between two wires for power lines.
2. A method for the autonomous installation of spacers with the proposed end effector using magnetic-field-based localization.

Existing robotic power line devices are primarily for maintenance and monitoring purposes, requiring manual attachments to the wire [6,7]. Attachment to the wire is accomplished by various mechanisms, ranging from parallelogram linkages [8] to novel clamping devices [9] and v-shaped two-point slots [7,10].

In our previous work [11], we presented a charging station for power lines and a corresponding end effector designed to install the charging station on the line. In [12,13], the authors presented the mechanisms for the installation and removal of aircraft warning spheres on power lines.

Unlike the previously presented solutions, the end effector presented here is intended for use with two parallel power lines.

The idea of using localization based on magnetic field measurements has been implemented for unmanned aerial vehicles (UAVs) that perch on power lines to recharge and thus extend their mission duration [14]. In [15], the authors investigated how to compute the position and orientation of UAVs with a minimum number of only three 3-axis magnetometers in the vicinity of two parallel power lines. However, this is not feasible in the application studied due to the specific design of the end effector and the pattern required to position the sensors. The same approach was experimentally validated in our previous work [16], together with the numerical localization method for two wires. In [17], a deep learning neural network architecture for precise indoor magnetic localization was developed to demonstrate the potential of precise magnetic positioning using smartphone sensors alone. In [17], the authors questioned the feasibility of indoor magnetic localization and concluded that the most effective localization occurs in close proximity (10 cm) to the magnetic field. The work in [18] presented simultaneous indoor localization and mapping based on the electromagnetic field of a building's power grid. In [19], a robust electromagnetic sensing system for 6-DOF pose estimation was presented, which can be useful for indoor localization and UAV landing scenarios, especially under challenging conditions. Considering some other application areas (e.g., medical), magnetic positioning technology is a suitable method for capsule localization in endoscopy [20]. Considering logistics systems and, in particular, automated warehouses, magnetic positioning can serve well as a guidance method for automated guided vehicles (AGVs) [21].

As for the work related to autonomous object handling, the basics of visual servoing are presented in [22]. Park et al. [23] designed a system that enables image-based visual servoing without prior depth information. The center of the target object is localized at the principal point of a camera. Using iterative lateral motion and one monocular camera, depth can be estimated. This paper shows that, with estimated depth and image-based visual servoing, it is possible to grasp an object. Gong et al. [24] presented a projective homography-based uncalibrated visual servo approach. This presented approach is capable of both static positioning and dynamic tracking tasks for systems with unknown intrinsic camera parameters and eye-hand relationships. In [25], a 3D electromagnetic motion control servo system with magnetic flux density feedback was developed for operation in non-line-of-sight environments. Such a system demonstrates the ability to control complex engineering systems based on magnetic field measurements. In [26], an endoscope with a magnetically anchored and guided system (MAGS) for minimally invasive surgery was presented. In [27], the visual-servo-based automatic tracking of a MAGS soft-body endoscope was achieved for the first time. In this case, a convolutional neural network (CNN) was used as a continuous visual servo controller. Such CNNs use only the reference image of the object and the current image of the camera to regress the control signal for the robot manipulator. To the best of our knowledge, this is the first paper in the field that deals with autonomous electrical spacer installation based on a special end effector and magnetic localization with a robotic manipulator. Moreover, the novel result is reinforced by the fact that this is the first autonomous installation of the device on power lines using magnetic localization.

The present paper is divided into six sections. Section 2 describes the design of the dedicated tool for the automated installation of electric spacers. Section 3 contains a problem definition, describes robot manipulator control modes, and presents a state machine for autonomous electrical spacer installation. Section 4 presents a method for the magnetic localization of power lines based on magnetic field measurements. Section 5 presents the hardware used and the experiments we performed to verify our method. In Section 6, we present lessons learned and system limitations. Section 7 summarizes the findings and results obtained.

## 2. End Effector for Spacer Installation

In this section, we present electrical spacer and specialized end effector designs for autonomous spacer installation.

### 2.1. Electrical Spacer

An electrical spacer is a mechanical device that keeps two, three, or four power lines at a constant distance from each other. Its purpose is to prevent short-circuiting between power lines and to dampen power line vibrations under harsh weather conditions. There are various designs of electrical spacers produced by different manufacturers.

This paper deals with the autonomous installation of electrical spacers for two wires shown in Figure 2. It consists of a spacer body, two bolts with rubber dampers, and two lower jaw parts. The bolt clamps the conductor between the spacer body and the jaws on each side. From Figure 2, it can be seen that when the spacer is open, the spacer jaws are free to move in all directions around the bolt that holds them.



**Figure 2.** Two-wire electrical spacer (top image), unscrewed lower jaw (left bottom image), and rotated lower jaw (right bottom image).

The selected spacer is designed for manual installation by the maintenance crew. The procedure for manually installing the electrical spacers is to position the conductor between the jaws and the spacer body, then tighten the bolts by hand while adjusting the position and orientation of the jaws with the other hand. The same procedure is repeated on the other side of the spacer. This type of electrical spacer is manufactured for different distances between conductors, ranging from 300 to 600 mm. Such electrical spacers are not adaptable to different distances but are rather manufactured for certain predefined distance.

### 2.2. Design of the End Effector

The special end effector is designed for autonomous installation based on the construction of the electrical spacer. The design of the end effector for the installation of electrical spacers must adapt to the requirements defined by the design of the spacer, namely:

- Keeping the spacer jaws open prior to installation;
- Tightening the bolt;
- Releasing the spacer when the installation is finished;
- Providing adaptability for spacers of different lengths.

There is another requirement that the end effector must adapt to. According to the specification for the robot arm, the end effector must comply with a weight limit of 5 kg total weight, including the electrical spacer. The heaviest mass of the electric spacer predicted in this work is 1.5 kg. Thus, the mass of the end effector must be less than the limit of 3.5 kg.

Each of these points is addressed by the design of the newly developed end effector. Its model and model components are shown in Figure 3.

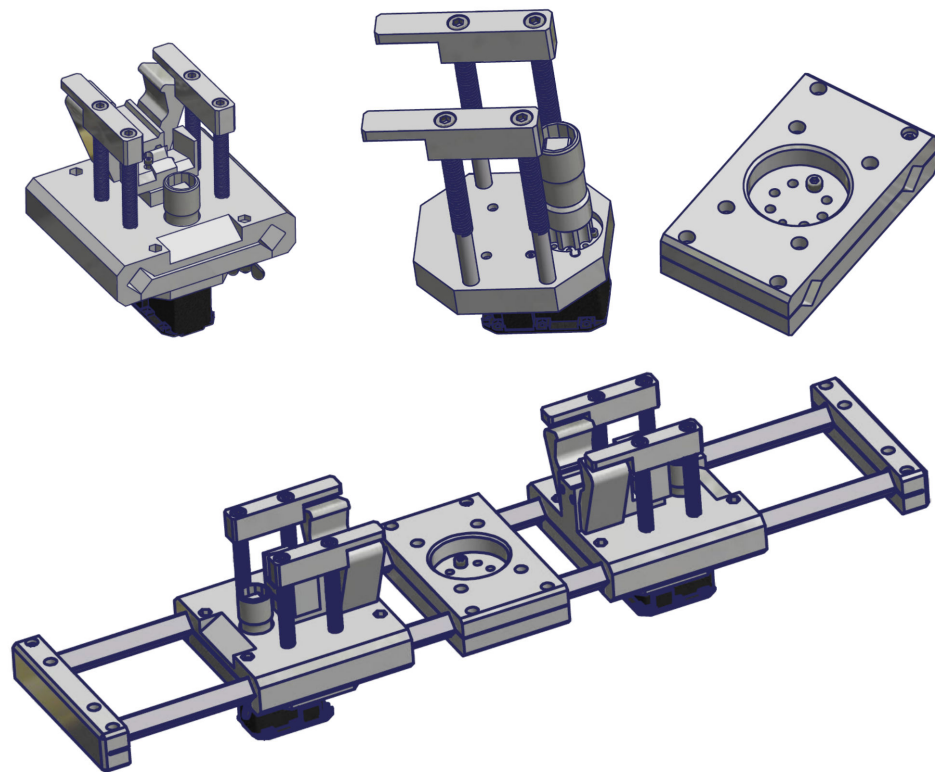


**Figure 3.** Model of the end effector for installation of electrical spacers. Side-operating sub-assembly that holds spacer jaw and tightens it (**top left** image). Motor plate and screw wrench (bolt tool) are used to tighten spacer jaw and they are a part of the side-operating sub-assembly (**top center** image). End effector adapter is used to connect end effector to robot arm flange (**top right** image). Complete rendered CAD model of the proposed specialized end effector for spacer installation (**bottom** image).

To accommodate the varying lengths of the spacer, the end effector is divided into three distinct subassemblies (see Figure 3). Two subassemblies are identical and are designed to operate the opposite sides of the spacer, while the third subassembly of the end effector is designed to be positioned between these two identical subassemblies and is prepared for installation on the robot arm flange. All three subassemblies are designed to run on two guides that hold all three parts as a whole. Each of these subassemblies can be fixed at any point on the guides, so that the spacers of different length can be installed.

Prior to installation, the spacer jaws must be held open (see Figure 2) to allow the spacer to enclose the conductors of the power line. This is achieved by holding the initial part of the jaws pressed with a spring (see Figure 4).

The bolts are tightened by an electric motor mounted on the bottom of the end effector. The electric motor is mounted on the movable plate, which is connected to the rest of the end effector by a shaft holding the bolt tool and four rods with springs on the top of the end effector (see Figure 4). These springs push the plate towards the rest of the end effector with a certain amount of force. This force ensures that the shaft with the bolt tool is pressed onto the bolt as the bolt is tightened. Since the upper part of the spacer is fixed in the end effector, the jaws start to close when the bolt is tightened, and the bolt moves towards the fixed part of the spacer.

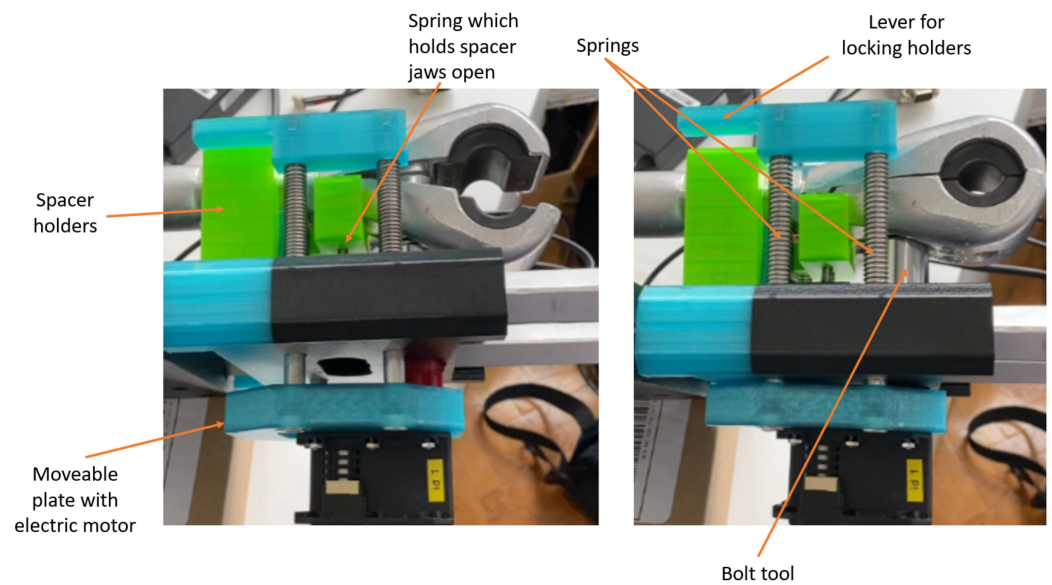


**Figure 4.** Main parts of the electrical spacer installation mechanism. Left image shows untightened bolt and spacer jaw open (prior to installation). Right image shows tightened bolt and spacer jaw closed (installed).

To hold the electrical spacer in the end effector, there are two holders on each side that hold the spacer while it is transported to the installation site. The two holders on each side are connected by a spring that ensures they are closed when in an idle state. During transport, the holders are additionally locked by a lever mounted on the rods of the motor plate (see Figure 4). In this way, they cannot be opened accidentally during the transport phase. When the spacer bolts are tightened, the rods and the lever are moved upwards, and in an instant, the lever moves above the level of the holder so that the holders can open. In this way, the holders are unlocked when the spacer is installed on the power line, and the end effector can be removed from the spacer.

The design process for such a compact, smart product in the form of a specialized end effector must be carried out in several iterative steps. In these steps, the number of actuators, the shape of the parts, and the mass of the parts are optimized. In the functional analysis, 14 functions are identified that require a force source for the movement:

- Increasing/decreasing the distance between opposing operating side subassemblies;
- Locking/unlocking the operating side subassembly position;
- Gripping/releasing the electrical spacer;
- Locking/unlock the electrical spacer;
- Opening/closing the electrical spacer jaw (releasing/tightening the spacer bolt);
- Moving the bolt tool on the bolt head along the bolt axis in both directions;
- Keeping/releasinh the electrical spacer jaw in the open position.

Optimization was provided using the designers' xperiences upgraded on theoretical backgrounds. The optimization focuses on the versatile use of the force sources and the shape of the subassembly parts. Some of these functions are performed manually on the ground.

### 2.2.1. Position of the Subassembly on the Guides

The side operating subassembly (see Figure 5) is locked onto the guides by the frictional force caused by two screws that tighten the clamp (lower part). The hexagonal bolt in the hexagonal hole and the wing nuts allow tightening and loosening without additional tools (see Figure 5). The clearance between the upper part and the guides allows the movement of the side operating subassembly along the guides when the screws are loosened. When

the screws are tightened, the clamp pushes the guides to the upper part, and the position is fixed.

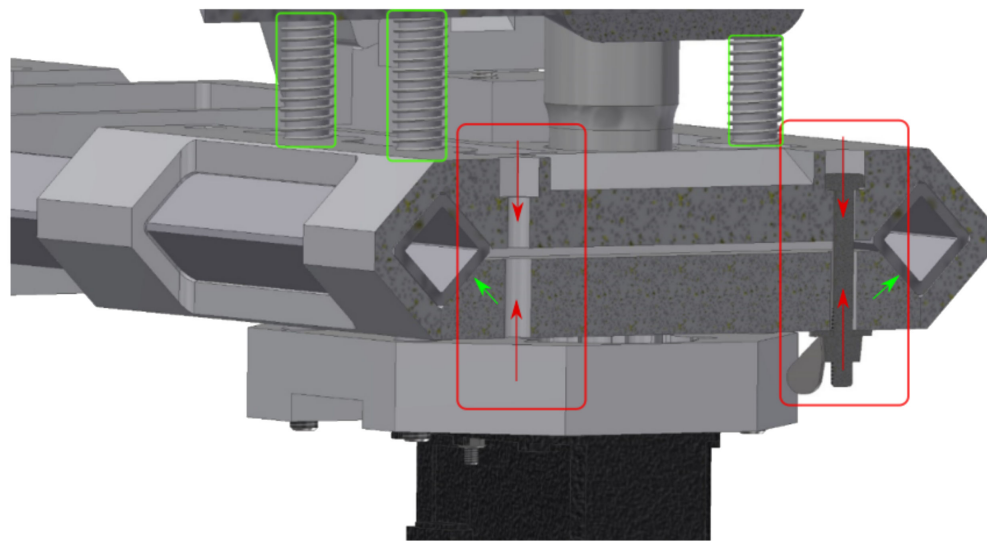


**Figure 5.** Side operating subassembly position adjustment mechanism. The red arrows show force achieved by two screws tightened by clamp (red rectangles). The green arrows show the acting normal force. The green rectangles show springs, which connect the locking holders and movable plate with electric motor (tightening mechanism).

### 2.2.2. Holding and Locking the Spacer in the End Effector

The spring is used to create a minimal force that closes the electrical spacer holders. Opening and closing of the holder is accomplished by rotating the holder about a z-axis, as shown in Figure 6. Gripping the electric spacer is done manually on the ground, which means that the in-air autonomous release of the electrical spacer is more critical. During the release, the electrical spacer is connected to the power lines, and the power line is used as the reaction force source, while the robot arm is used as the active force source in the vertical downward direction. This implies that the active force holding the electrical spacer in the end effector must be as small as possible. Minimizing this force is achieved by:

- Taking advantage of the shape of the electric spacers;
- Using two oppositely directed holders;
- Optimizing the position of the axis of rotation of the holder;
- Optimizing the shape of the holder.

The electric spacer holders are positioned on the hexagonal shape near the spacer jaw. When the upper force on the holder is vertical, its position leads to the opening of the holder. At this moment, the spring force is as low as possible, and the action and reaction force is also as low as possible. At the second moment, while the spring force is slowly increasing, the upper force on the holder changes its direction. At this moment, most of the normal force is absorbed by the solid body of the electric spacer, while the action and reaction force sources absorb most of the much smaller frictional force. The position of the electrical spacer must be fixed in the end effector while the robot arm is moving. While the robot arm is moving, the spacer jaws must remain open prior to installation. The electrical spacer can be unlocked from the end effector when the electrical spacer is installed on the power line. The electrical spacer is installed when the jaws are closed (the bolt is tightened and the bolt head is in the up position), and the conductor passes through the clamping jaws. The same force can be used for all functions:

- Locking/unlocking the electrical spacer;
- Moving the bolt tool on the bolt head along the bolt axis in both directions.

The hexagonal shape of the electrical spacer and holders all around it stabilize its position. The extended tightening mechanism yoke allows the position of the spacer to be locked when the end effector is in the air and unlocked when the end effector is on the ground or the electrical spacer is installed.

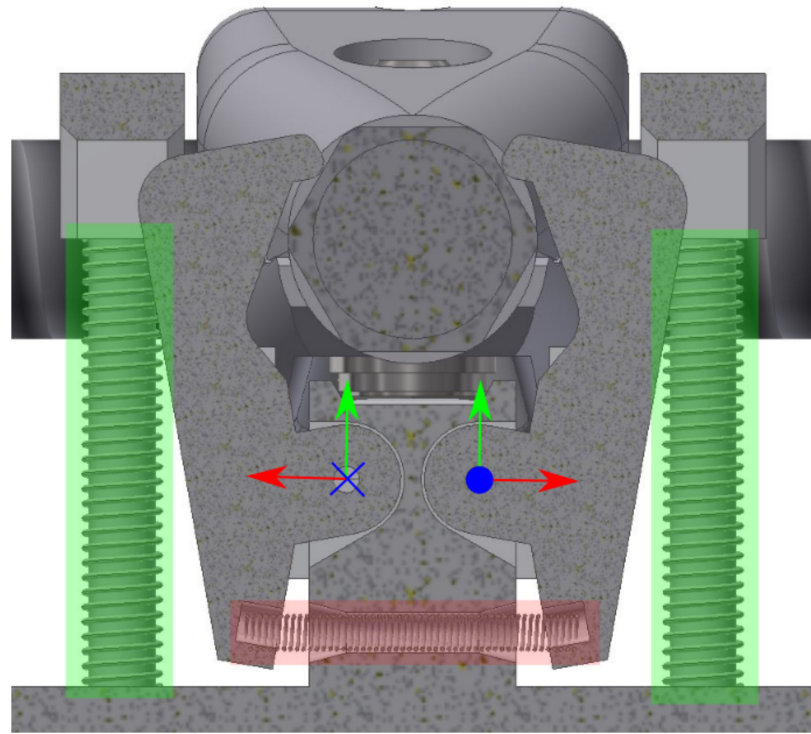


**Figure 6.** Electrical spacer holder mechanism. The red rectangle shows spring that generates closing force. Coordinate systems show z-axis (blue) around which both holders rotate. Green rectangles show the springs of the tightening mechanism.

### 2.2.3. Closing the Electrical Spacer

Closing the electrical spacer jaw (screw bolt) is the main function of the special end effector that has been developed. This function is performed by rotating the spacer bolt around its axis until the target torque is reached (the target torque is determined empirically by measuring the motor current and finding the current limit, which corresponds to the torque reached when the jaws are closed). The electric motor with the mounted bolt tool serves as the force source for opening and closing the jaws (tightening/releasing the spacer bolts). Tightening/releasing the spacer bolts leads to the movement of the bolt head along the bolt axis, which the bolt tool must follow. Opening the electrical spacer jaw (releasing the spacer bolt) pushes the bolt tool down. Contact between the bolt tool and the spacer bolts must be ensured when the electrical spacer jaw is closing. The movement of the electric motor and the bolt tool must be guided. Round tubes guided by holes in the main support part of the side operating subassembly are used to ensure this guidance. Four springs around those tubes supported with the main supportive part on one end and tightening mechanism yokes on the other end are used to ensure contact between the bolt tool and the spacer bolt. The tightening mechanism yokes are connected with long bolts through tubes to the support part of the electric motor. The electric motor with the bolt tool is attached to the support part with six bolts. All together, this comprises the tightening mechanism that moves along the axis of the spacer bolt axis while opening/closing the spacer jaws.

The critical point of the tightening mechanism design is the guidance. The mechanism is symmetrical with respect to the electrical spacer (red dashed line in Figure 7), but



optimization is required to minimize rotation about the perpendicular axis on the electrical spacer and increase the frictional force of the guidance.

There are three forces that must be considered: the resultant action force of the springs, the passive gravity force of the mass, and the reaction force of the spacer bolt on the bolt tool (see Figure 7). With shape optimization, the position of the gravity force (center of mass without springs) and the position of the resultant force of the springs (corresponding to the center of mass of the springs) are approximated as much as possible. These two force components result in a minimal frictional force when guiding the bolt tool. When the electrical spacer jaw is closed (spacer bolt up), the spring force must be as small as possible. This results in minimal reaction force on the bolt tool as well as minimal friction force during its guidance. The torque of the electric motor is used to tighten the bolt. When the electrical spacer jaw is open (spacer bolts are in the lower position), the spring force slowly increases. As the spring force increases, the reaction force on the bolt tool and the frictional force for bolt tool guidance also increase. The electric motor is able to overcome the reaction and friction force, and the tightening mechanism moves and works as expected. The whole system works only if the jaws of the electrical spacer are in the open position until the electrical spacer is installed on the power lines. It is possible to evaluate the installation procedure phase (installed/not installed) based on the value of the current measurement of the electric motors used whilst tightening the bolt of the tightening mechanism.

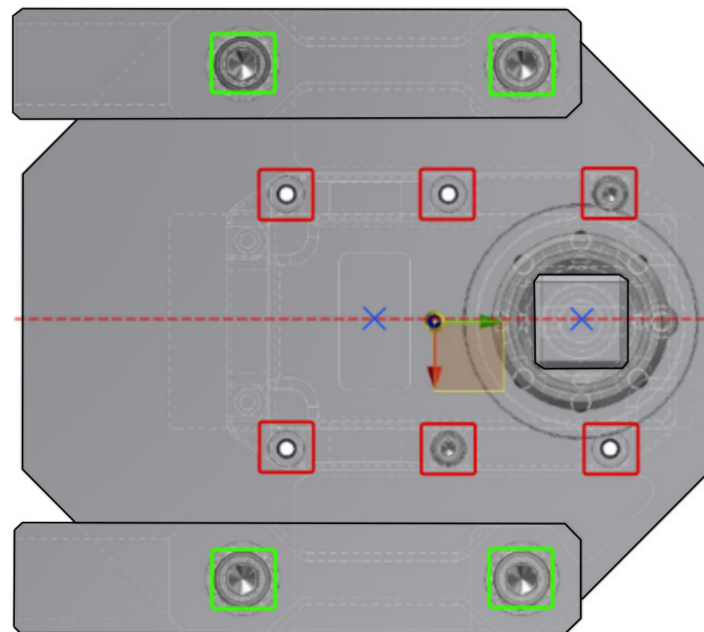


**Figure 7.** Tightening mechanism with center of mass. The red rectangles show six bolts that fix the motor and the bolt tool on support part. The dashed red line shows the electrical spacer axis. Green rectangles show position of the four springs of the tightening mechanism. Left blue X shows resultant action force of the springs, and the right blue X shows reaction force of the spacer bolt on the bolt tool.

#### 2.2.4. Keeping Electrical Spacer Jaw in the Open Position

The electrical spacer and the spacer jaw have slots that allow the jaws to be held in the open position by the operator's thumb during manual installation (see Figure 8). In the special end effector described in this paper, the operator's thumb force is replaced by the force of two springs. This force must be as small as possible so that it does not effect the tightening mechanism, the guidance, the friction force, or the spacer bolt axial force. In order to prevent an effect from an accidental lateral force on the electrical spacer jaw, the thumb replacement part has a limiter on each side and an optimized multi-purpose shape. The optimization of the spring force and interactive force position renders negative effects on the guidance of the tightening mechanism negligible.

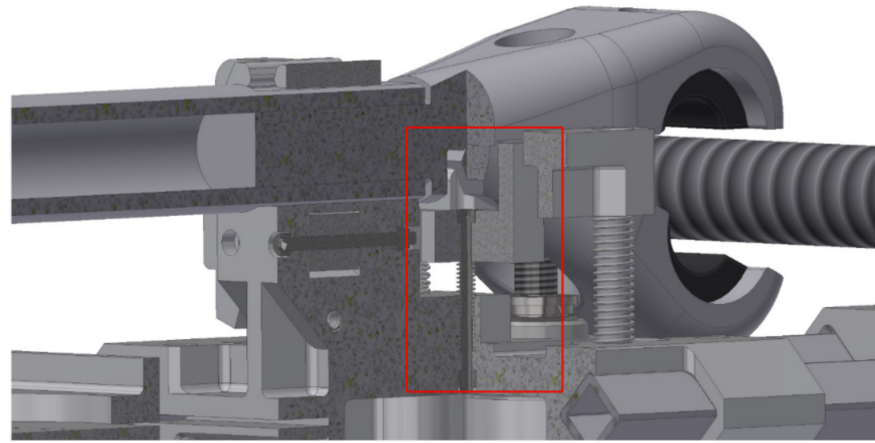


**Figure 8.** The thumb replacement mechanism.

The shapes of the multi-purpose parts and the multi-purpose force sources are achieved through multiple iterations of the optimization process. The result is our special end effector for the autonomous installation of electrical spacers that can be easily fabricated and functions properly. This approach, combined with weight requirements, makes additive technology the best choice for manufacturing most parts. Additive technology, when used in production, requires modeled mechanical component tolerances. The end effector mechanisms produced by additive technology, where different parts interact, require continuous optimization of part tolerances during product design to function properly. All these processes are successfully performed and presented in this work.

### 2.3. Prototype

The fabricated prototype is shown in Figure 9. Due to its multipurpose shape and weight limit, most of its parts are 3D printed using polylactic acid (PLA) material. Its guide elements (square and round tubes) are AlMgSi0, its five springs are WNr1.1200, and its standard screws are zinc-galvanized. The actuators used for actuating the end effector are Dynamixel MX64 (basic parameters of Dynamixel MX64 are presented in Table 1).

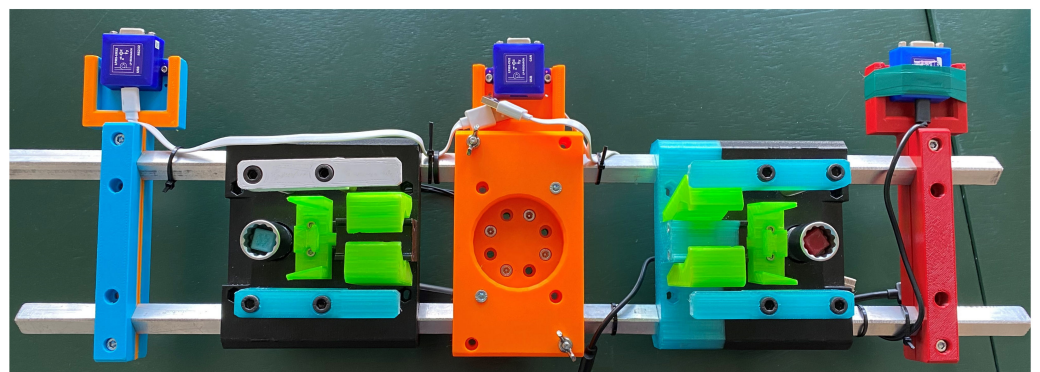


**Figure 9.** The prototype of the end effector for the installation of the electrical spacers.

The whole production and assembly of the presented prototype of a specialized end effector for autonomous electrical spacer installation is carried out by additive technology (3D printing) and hand tools. The achieved weight of the prototype is approximately 2.3 kg, which is less than 2/3 of the target weight limit of 3.5 kg.

The end effector is designed to approach the power lines from below, and when it reaches the desired height, it is rotated so that the spacer surrounds the lines on both sides. The actuators tighten the bolt to close the jaws of the spacer. When the spacer closes on the conductor, the end effector is unlocked from the spacer and can be removed by pulling it

downwards. Figure 10 shows the procedure for installing the electrical spacers on power lines.

**Table 1.** Basic parameters of Dynamixel MX64 servo motor.

Item	Specification
Motor	Coreless (Maxon)
Weight	126 g
Gear ratio	200:1
Stall torque	6.0 Nm on 12 V
No load speed	63 rev/min at 12 V
Communication interface	RS485

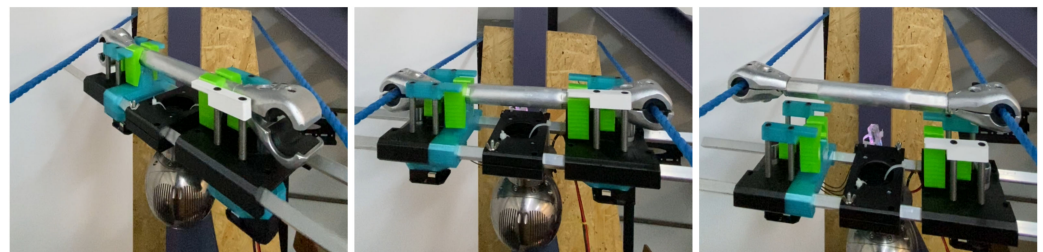


**Figure 10.** Sequence of images showing the end effector from the preinstallation pose  $x_{pp}$  (left image), installation pose  $x_{ip}$  (center image), to the installed spacer on powerlines (right image).

### 3. Robot Control Problem Statement

From a control perspective, the procedure for installing the spacer is divided into three tasks, which are carried out sequentially in three logical steps. Since the end effector must approach the wires from below, the first step is to position the end effector with the spacer in the approach pose, i.e., below the wires. The second step involves servoing based on magnetic-field-based localization towards the preinstallation pose, which is defined by the spacer being positioned between, at the same height as, and almost parallel to the wires. The third step involves rotating the spacer (end effector) so that the jaws of the spacer enclose the wires on both sides. This procedure is shown in Figure 11. For the installation, we use a 6DOF robot arm Schunk LWA4p. A complete kinematic (forward, inverse) derivation of the robotic arm can be found in [28].

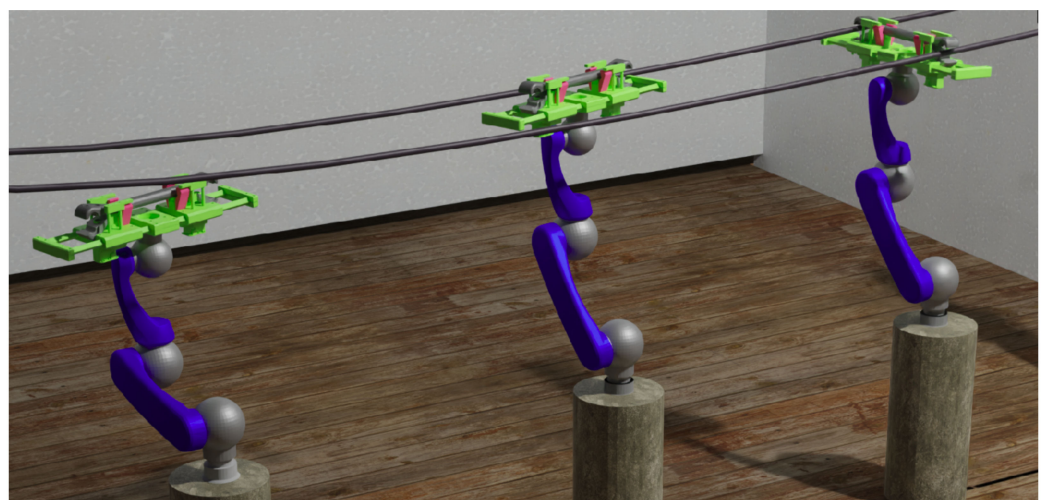


**Figure 11.** Robotic arm with the special end effector rendered in the approach pose ( $x_{ap}$ ), preinstallation pose ( $x_{pp}$ ), and the installation pose ( $x_{ip}$ ) (from left to right).

### 3.1. Approach Pose

The first step consists of positioning the robot manipulator with the corresponding end effector in the approach pose, defined by:

$$\mathbf{x}_{ap} = [x_{ap} \ y_{ap} \ z_{ap} \ q_{ax} \ q_{ay} \ q_{az} \ q_{aw}]^T \tag{1}$$

where  $x_{ap}$ ,  $y_{ap}$ , and  $z_{ap}$  define the position of the approach pose and  $q_{ax}$ ,  $q_{ay}$ ,  $q_{az}$ , and  $q_{aw}$  define the quaternion that represents the orientation of the approach pose. If we define two parallel conductors as two lines in 3D, they can be described by the following equations:

$$\begin{aligned} \mathbf{p}_{pl}^1 &= \mathbf{p}_{pl0}^1 + \mathbf{v}_{pl}s^1 \\ \mathbf{p}_{pl}^2 &= \mathbf{p}_{pl0}^2 + \mathbf{v}_{pl}s^2 \end{aligned} \tag{2}$$

where  $\mathbf{p}_{pl}^1 = [x_{pl}^1 \ y_{pl}^1 \ z_{pl}^1]^T$  defines the points of a first line,  $\mathbf{p}_{pl}^2 = [x_{pl}^2 \ y_{pl}^2 \ z_{pl}^2]^T$  defines the points of a second line,  $\mathbf{p}_{pl0}^1 = [x_{pl0}^1 \ y_{pl0}^1 \ z_{pl0}^1]^T$  is one point on the first line,  $\mathbf{p}_{pl0}^2 = [x_{pl0}^2 \ y_{pl0}^2 \ z_{pl0}^2]^T$  is one point on the second line,  $\mathbf{v}_{pl} = [v_{xpl0} \ v_{ypl0} \ v_{zpl0}]^T$  is a line direction vector common for both lines, and  $s^1$  and  $s^2$  are scalars. The origin of the approach pose is chosen based on the points on each conductor (defined as a line in Equation (2)) closest to the robot base, i.e., the origin of the global coordinate frame  $\mathbf{x}_G$  [29]:

$$\begin{aligned} \mathbf{p}_{C1} &= \mathbf{p}_{pl0}^1 + \mathbf{v}_{pl}(\mathbf{p}_{pl0}^1 \cdot \mathbf{v}_{pl}) \\ \mathbf{p}_{C2} &= \mathbf{p}_{pl0}^2 + \mathbf{v}_{pl}(\mathbf{p}_{pl0}^2 \cdot \mathbf{v}_{pl}) \end{aligned} \tag{3}$$

where  $\mathbf{p}_{C1} = [x_{pc}^1 \ y_{pc}^1 \ z_{pc}^1]^T$  is the point on the first line closest to the origin of  $\mathbf{x}_G$  and  $\mathbf{p}_{C2} = [x_{pc}^2 \ y_{pc}^2 \ z_{pc}^2]^T$  is the point on the second line closest to the origin of  $\mathbf{x}_G$ . The origin of the approach pose is calculated by:

$$\begin{aligned} x_{ap} &= (x_{pc}^1 + x_{pc}^2)/2 \\ y_{ap} &= (y_{pc}^1 + y_{pc}^2)/2 \\ z_{ap} &= (z_{pc}^1 + z_{pc}^2)/2 - a_{tl} - o \end{aligned} \tag{4}$$

where  $o$  is the initial offset along the  $z$  axis from the spacer to the wires and  $a_{tl}$  is the distance along the  $z$  axis from the last robot joint to the electrical spacer. The quaternion defined by  $q_{ax}$ ,  $q_{ay}$ ,  $q_{az}$ , and  $q_{aw}$  is determined from  $\mathbf{v}_{pl}$ , taking into account the following assumptions:

- Power lines are parallel to the ground;
- Power lines are the same height from the ground.

This implies that the orientation of the power lines is defined only by a yaw angle:

$$\gamma = \arctan\left(\frac{y_{pl0}}{x_{pl0}}\right) \tag{5}$$

where  $\gamma$  is the yaw angle of the conductors. The yaw angle of the end effector is defined by:

$$\psi = \gamma + \psi_o \tag{6}$$

where  $\psi_o$  is a small offset added to avoid positioning magnetometers parallel to the conductors. By simple conversion, the end effector yaw angle  $\psi$  can be transformed into the quaternion  $(q_{ax}, q_{ay}, q_{az}, q_{aw})$ .

### 3.2. Preinstallation Pose

Starting from the approach pose, we use magnetic localization and servo control of the robot arm to position the end effector between the conductors in the preinstallation pose. The preinstallation pose is defined as follows:

$$\mathbf{x}_{pp} = [x_{pp} \quad y_{pp} \quad z_{pp} \quad q_{px} \quad q_{py} \quad q_{pz} \quad q_{pw}]^T \quad (7)$$

where

$$\begin{aligned} x_{pp} &= (x_{pc}^1 + x_{pc}^2)/2 \\ y_{pp} &= (y_{pc}^1 + y_{pc}^2)/2 \\ z_{pp} &= (z_{pc}^1 + z_{pc}^2)/2 - a_{tl} \end{aligned} \quad (8)$$

The quaternion  $(q_{px}, q_{py}, q_{pz}, q_{pw})$  is determined from the desired yaw angle  $\psi_{pp} = \gamma + \psi_0$ .

### 3.3. Installation Pose

After positioning the end effector in the preinstallation pose between the power lines, we must perform the necessary rotation of the tool to position the spacer vertically and drop the conductors between the jaws of the spacer, as shown in Figure 10. This pose is called the installation pose, and it is defined as:

$$\mathbf{x}_{ip} = [x_{ip} \quad y_{ip} \quad z_{ip} \quad q_{ix} \quad q_{iy} \quad q_{iz} \quad q_{iw}]^T \quad (9)$$

where the quaternion  $(q_{ix}, q_{iy}, q_{iz}, q_{iw})$  is calculated from the desired yaw angle  $\psi_{ip} = \gamma + \pi/2$ .

Figure 11 shows, from left to right,  $\mathbf{x}_{ap}$ ,  $\mathbf{x}_{pp}$ , and  $\mathbf{x}_{ip}$  in relation to the power lines.

The next step is to close the jaws of the spacer around the conductor by the actuators of the end effector. The spacer is considered closed and the actuator is stopped when its current rises above a certain threshold value for a certain amount of time:

$$I_{mc} > I_{cl} \quad (10)$$

where  $I_{mc}$  is the actuator current and  $I_{cl}$  is the current limit at which the spacer is considered closed.

### 3.4. Motion Planning and Trajectory Execution

For motion planning and trajectory execution, we use MoveIt! [30] <https://moveit.ros.org/> (accessed on 11 February 2023), developed by: <https://picknik.ai/> (accessed on 11 February 2023), ROS <https://www.ros.org/> (accessed on 11 February 2023), and Gazebo <http://gazebosim.org/> (accessed on 11 February 2023) to safely plan a collision-free path of motion. We use OMPL [31] as a motion planning library and Rapidly Exploring Random Trees (RRT) as part of MoveIt! for planning. We added an end effector model in URDF and power lines to the planning scene to enable the collision-free execution of the trajectory.

### 3.5. Robot Arm Servoing

After reaching the approach pose, the servo control of the robot arm is used to reach the preinstallation pose. The servo control of the robot arm is realized with four P-controllers and the MoveIt! servo ROS package.

The difference between the current pose of the end effector and the preinstallation pose, which is calculated based on the current estimation of the power line position, is used as an input signal for the P-controllers. Three P controllers are used to track the end effector's position (see Equations (11)–(13)), while one P controller is used to track the end effector's orientation (see Equations (14)–(18)). The output of each P controller depends on the gains  $(K_{px}, K_{py}, K_{pz})$  and the error, which is calculated as the difference of the

commanded value for each axis(  $x_{cmd}, y_{cmd}, z_{cmd}$ ) and the measured end effector pose ( $x_{ee}, y_{ee}, z_{ee}$ ) for each axis.

$$\dot{x}_e = K_{px}(x_{cmd} - x_{ee}) \quad (11)$$

$$\dot{y}_e = K_{py}(y_{cmd} - y_{ee}) \quad (12)$$

$$\dot{z}_e = K_{pz}(z_{cmd} - z_{ee}) \quad (13)$$

while one P controller is used to control the end effector orientation. The orientation error is determined as the product between the desired orientation quaternion  $\mathbf{q}_{des}$  and the inverse quaternion of the current end effector orientation  $\mathbf{q}_{ee}$  [32],

$$\mathbf{q}_e = \mathbf{q}_{des}\mathbf{q}_{ee}^{-1}. \quad (14)$$

The orientation error quaternion is converted into an axis  $[e_x, e_y, e_z]$  and an angle ( $\theta_e$ ) representation. Using this angle and the P controller, the angle magnitude is computed as follows:

$$\theta_{mag} = K_{p\theta}\theta_e \quad (15)$$

Using the calculated axis, we can calculate angular velocity for the end effector, as follows:

$$\dot{\theta}_x = \theta_{mag}e_x \quad (16)$$

$$\dot{\theta}_y = \theta_{mag}e_y \quad (17)$$

$$\dot{\theta}_z = \theta_{mag}e_z \quad (18)$$

The first three P controllers are used to generate the control input to reach the desired end effector position, as shown in Equations (11)–(13). We assume that the magnetic estimation will be correct enough that the commanded position will not lead the system to instability; furthermore, we set  $K < 1$  in order to slow down the continuous arm movement to the commanded position. We experimentally evaluated that adding a  $K_i$  or  $K_d$  component to the control loop for robot arm servoing leads to the degraded performance of the controller.

The fourth P controller controls the magnitude of orientation error, as shown in Equation (15). The magnitude of the orientation angle error is used to calculate angular velocity for each end effector axis, as shown in Equations (16)–(18). The outputs of the four P controllers with gains  $K_{px}, K_{py}, K_{pz}$ , and  $K_{p\theta}$  determine the velocity of the end effector in the task space. Robotic arm servoing is implemented using the Jacobian pseudoinverse, as shown in [30]. Robot arm servoing control structure can be seen in Figure 12.

We try to exploit the fact that the magnetic field measured by the magnetometers is stronger the closer the end effector is to the power lines. Therefore, the localization becomes more accurate and precise as the error between the tracked pose and the current pose of the end effector decreases.

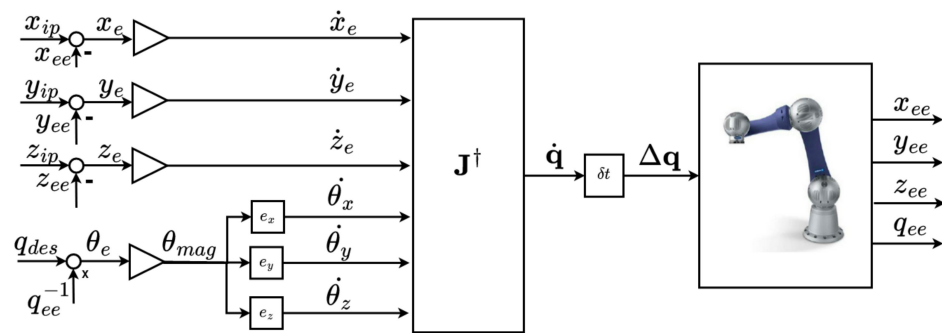


**Figure 12.** Control diagram for the robot arm servoing.  $\mathbf{q}_{des}$  and  $\mathbf{q}_{ee}$  depict desired and current end effector orientation in quaternions.  $\dot{\mathbf{q}}$  is vector of the joint velocities,  $\delta t$  is discretization period used, and  $\Delta \mathbf{q}$  is the desired change in joint position.  $x_{ip}$ ,  $y_{ip}$ , and  $z_{ip}$  represent commanded end effector position for  $\mathbf{x}_{ip}$ .  $x_{ee}$ ,  $y_{ee}$ , and  $z_{ee}$  are the end effector position.  $\mathbf{J}^{\dagger}$  is Jacobian pseudoinverse.

### 3.6. State Machine

We have developed a finite state machine that divides the process of installing the electrical spacer on power lines into logical states that are also the sequential tasks of the entire process. The installation process is divided into two superstates and two final states. The superstates are called the stationary arm and the moving arm.

Each superstate contains multiple states. The moving arm superstate contains states that require robot arm movement, such as trajectory execution, servoing, and rotating the tool. The stationary arm superstate contains all states in which the robot arm is stationary, such as the initial pose, the approach pose ( $\mathbf{x}_{ap}$ ), the preinstallation pose ( $\mathbf{x}_{pp}$ ), the installation ( $\mathbf{x}_{ip}$ ) pose reached, and the install spacer. In addition to superstates, we define two final states that correspond to successful and failed spacer installation tasks. The state transition from the initial pose to trajectory execution is triggered with a command that contains the pose  $\mathbf{x}_{ap}$ , a timeout parameter  $t_1$ , and the scalar distance  $d_1$ . The robot reaches its approach pose if the distance function  $d_f(\mathbf{x}_{cmd}, \mathbf{x}_{meas})$  between the commanded  $\mathbf{x}_{ap}$  and the measured end effector pose  $\mathbf{x}_{ee}$  is smaller than the distance  $d_1$  and if the current task execution time  $t$  is smaller than the timeout  $t_1$ .

The distance function is defined as the sum of the Euclidean norm of the pose vector position components and the quaternion distance of the pose vector orientation components. The quaternion distance is defined as  $1 - \langle q_1, q_2 \rangle$  where  $\langle \rangle$  presents the dot product between two quaternions. The distance function for the approach pose is defined in Equation (19).

$$d_f(\mathbf{x}_{ap}, \mathbf{x}_{ee}) = (\|\mathbf{x}_{ap1:3} - \mathbf{x}_{ee1:3}\|) + (1 - \langle \mathbf{x}_{ap4:7}, \mathbf{x}_{ee4:7} \rangle) \quad (19)$$

The rest of the state transitions and conditions can be inferred from Figure 13, which shows a Harel statechart [33] of the system.

Yellow rectangles depict superstates, white rectangles depict states, and red and green rectangles depict final states. The transitions between states are shown with arrows. Black text above a state transition arrow describes a command sent. A blue text above a state transition describes a condition that must be met for state transition. The state machine was implemented using smach\_ros [http://wiki.ros.org/smach\\_ros](http://wiki.ros.org/smach_ros) (accessed on 10 February 2023) and ROS actionlib <http://wiki.ros.org/actionlib> (accessed on 10 February 2023).

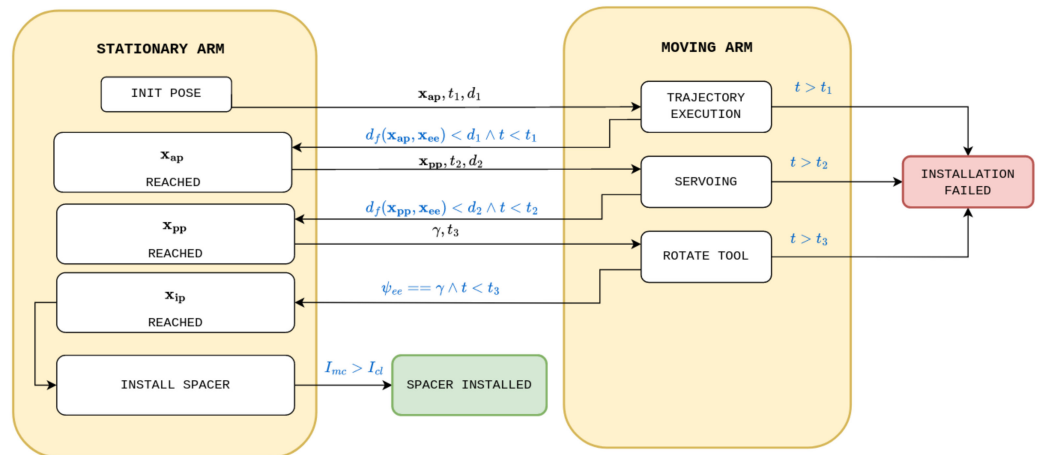


**Figure 13.** Harel statechart for the spacer installation task. The yellow rectangles represent superstates. The white rectangles are states, while the red and green rectangles are final states. The arrows indicate state transitions. The black text represents commands sent. The blue text represents conditions that must be met for the state transition.

#### 4. Localization of Power Lines

This section presents the numerical method for localization based on the magnetic field strength of two parallel straight conductors carrying the same current, similar to the one presented in [16].

##### 4.1. Magnetic Field Around the Conductor

The magnetic field strength produced by the flow of current through a long, straight conductor is:

$$B = \frac{\mu_0 I}{2\pi r} \tag{20}$$

where  $B$  is the strength of the magnetic field,  $\mu_0$  is the vacuum permeability,  $r$  is the distance from the conductor, and  $I$  is the conductor current.

Equation (20) provides the magnetic field strength at a distance  $r$ . The direction of the field is determined by the right-hand rule with respect to the conductor. Its vector always has a direction that is circumferential with respect to the isomagnetic lines.

The vector of the magnetic field  $\mathbf{B}(\mathbf{p}_0, I)$  at a point  $\mathbf{p}_0 = [x_0 \ y_0 \ z_0]^T$  generated by two parallel conductors (defined as 3D lines by Equation (2)) carrying the same current  $I$  can be calculated by:

$$\mathbf{B}(\mathbf{p}_0, I) = \mathbf{B}^1(\mathbf{p}_0, I) + \mathbf{B}^2(\mathbf{p}_0, I) \tag{21}$$

where  $\mathbf{B}^k$ , the magnetic field vector generated by one line,  $k$ , is:

$$\mathbf{B}^k(\mathbf{p}_0, I) = \frac{\mu_0 I}{2\pi |\mathbf{p}_0 - \mathbf{p}_{p11}^k|} \frac{(\mathbf{p}_0 - \mathbf{p}_{p11}^k) \times \mathbf{v}_{p1}}{|(\mathbf{p}_0 - \mathbf{p}_{p11}^k) \times \mathbf{v}_{p1}|} \tag{22}$$

where  $\mathbf{p}_{p11}^k$  is the point on the conductor  $k$  closest to the point  $\mathbf{p}_0$ , which can be calculated using Equation (2), with  $s^k$  calculated in the following way:

$$s^k = - \frac{(\mathbf{p}_{p10}^k - \mathbf{p}_0) \cdot \mathbf{v}_{p1}}{|\mathbf{v}_{p1}|^2} \tag{23}$$



#### 4.2. Numerical Method for Locating Two Power Lines Based on Three or More Magnetometers

At least three magnetometers at different locations are needed to locate two conductors [15]. Several assumptions have been made to avoid ambiguity and to increase the stability of the location determination:

- A-1 The conductors are parallel and at a distance  $d_c$  from each other;
- A-2 The distance from a magnetometer to the nearer conductor is less than  $d_{max}$ ;
- A-3 The current through the conductors will be less than  $I_{max}$ ;
- A-4 The conductors are parallel to the ground;
- A-5 The robot is never directly above the conductors;
- A-6 Two magnetometers must not be parallel with the conductors.

Assumption A-1 is usually satisfied if there is no strong wind. The assumptions A-2 and A-3 can always be satisfied for sufficiently large  $d_{max}$  and  $I_{max}$ . The assumption A-4 will not necessarily be satisfied under realistic conditions, but its angle will always be relatively small. Since the spacers are set up from below, A-5 can be assumed. If the magnetometers are placed parallel to the conductors, they will measure the same values, so A-6 must be satisfied for successful localization.

The measurements of all magnetometers  $\mathbf{B}_{mil}$  is measured in their frames  $\mathbf{M}_i$  defined by the vector  $\mathbf{T}_i$  and the rotation matrix  $\mathbf{R}$  (assuming the same orientation of all magnetometers) with respect to the global frame  $\mathbf{x}_G$ .

Under the assumption that both conductors are parallel to the ground, the direction of the conductors in  $\mathbf{x}_G$  (vector  $\mathbf{v}_{pl}$ ) for the setup with 3 magnetometers can be derived from the equation:

$$\mathbf{v}_{pl} = \sum_{i=1}^3 (\mathbf{B}_{mi} \times [0 \ 0 \ 1]^T) \quad (24)$$

where  $\mathbf{B}_{mi}$  is the measurement of magnetometer  $i$  expressed in the global coordinate frame:

$$\mathbf{B}_{mi} = \mathbf{R}\mathbf{B}_{mil} \quad (25)$$

A special case occurs when all magnetometers are in the same plane as the conductors when (25) is a null vector. However, this problem can be solved by the careful choice of the relative position of the magnetometers, and it is sufficient if at least one magnetometer is not in the same plane as the conductors.

For the case of three magnetometers and two conductors, the location of the conductors can be determined by minimising the criteria:

$$G(\mathbf{p}_{pl}^1, \mathbf{p}_{pl}^2, I) = \sum_{i=1}^3 |\mathbf{B}_{mi} - \mathbf{B}(\mathbf{p}_{mi}, I)| \quad (26)$$

where  $\mathbf{p}_{mi}$  is the location of magnetometer  $i$  in the global frame (see Figure 14).

The criterion (26) is defined with 7 variables (3 in  $\mathbf{p}_{pl}^1$ , 3 in  $\mathbf{p}_{pl}^2$ , and  $I$ ). Since it was assumed that the conductors are parallel to the ground plane and to each other at a known distance, and that  $\mathbf{p}_{pl}^1$  and  $\mathbf{p}_{pl}^2$  are arbitrary conductor points defined by (2), the number of variables can be reduced.

Two independent variables define  $\mathbf{p}_{pl}^1$ , but the vector perpendicular to  $\mathbf{v}_{pl}$  needs to be determined first:

$$\mathbf{v}_{plperp} = \mathbf{v}_{pl} \times [0 \ 0 \ 1]^T \quad (27)$$

where  $\mathbf{v}_{plperp}$  is a vector perpendicular to the  $\mathbf{v}_{pl}$  and  $z$  vectors. Now,  $\mathbf{p}_{pl}^1$  can be represented with variables:

$$\mathbf{p}_{pl}^1 = s_1 [0 \ 0 \ 1]^T + s_2 \mathbf{v}_{plperp} \quad (28)$$

where  $s_1$  and  $s_2$  are two scalar variables.

$\mathbf{p}_{p10}^2$  can be determined by:

$$\mathbf{p}_{p10}^2 = \mathbf{p}_{p10}^1 + d_c \mathbf{v}_{pl\text{perp}} \quad (29)$$

Given the Equations (22), (23), (28), and (29), Equation (26) becomes:

$$G(s_1, s_2, I) = \sum_{i=1}^3 |\mathbf{B}_{mi} - \mathbf{B}(\mathbf{p}_{mi}, I)| \quad (30)$$

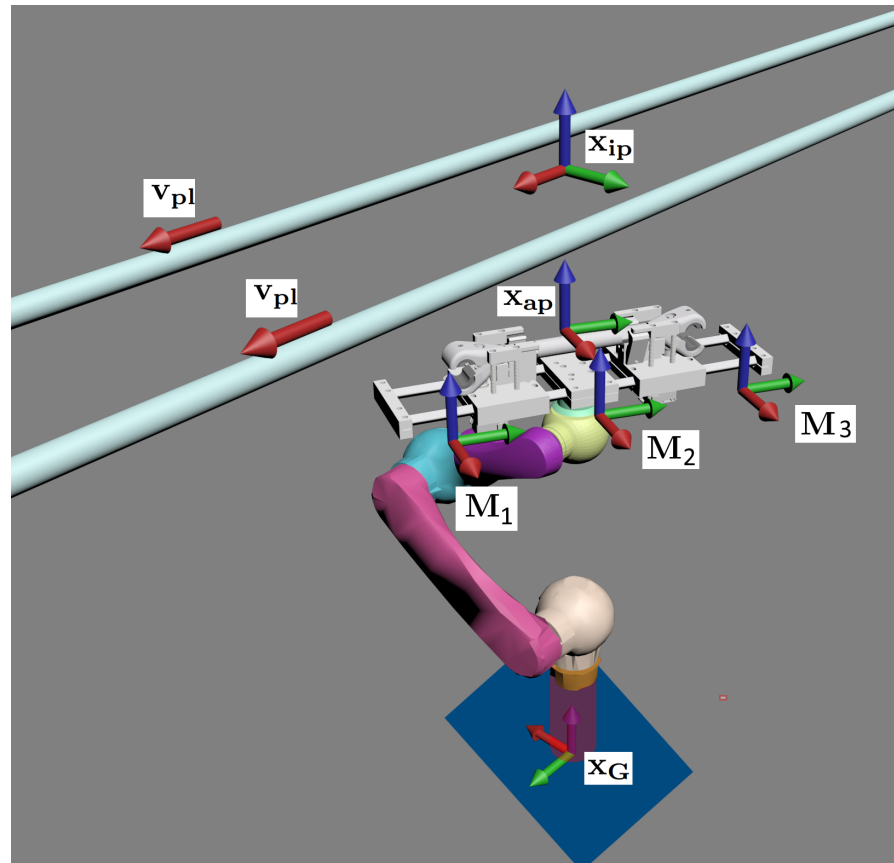


**Figure 14.** Coordinate frames used for localization and control. The red arrow represents the  $x$  direction, the green arrow represents the  $y$  direction, and the blue arrow represents the  $z$  direction.

The problem comes down to the minimization of three variable criteria. This minimization can be carried out by various methods. Due to the constraint of  $d_{max}$  and  $I_{max}$ , the optimal triplet  $s_1^*$ ,  $s_2^*$ , and  $I^*$  for criteria (30) will be within the range  $[-d_{max}, d_{max}]$ ,  $[-d_{max}, d_{max}]$ , and  $(0, I_{max}]$ , respectively. One way to find the optimal solution would be to discretize these ranges with the steps  $\Delta d$ ,  $\Delta d$ , and  $\Delta I$ , respectively, and go through all combinations of triplets  $(s_1, s_2, I)$ . After finding the triplet with the smallest criterion, further refinement around the triplet with the smallest criterion can be performed with steps  $\delta d$ ,  $\delta d$ , and  $\delta I$ .

#### 4.3. Processing the Measurements of the Alternating Magnetic Field

The first step in magnetic localization is processing the raw data collected by the magnetometers. Magnetometers measure magnetic fields, which are affected by various sources, such as the earth's magnetic field, the electric field of the power lines, noise from electric motors, etc. Since power lines generate an alternating magnetic field of known frequency (50 or 60 Hz), the first step is to estimate the amplitude and phase in the  $x$ ,  $y$ , and

$z$  directions of this field, which defines the influence of the power line. This information is then used in the further course of the localization procedure to determine the location of the power lines.

The measured magnetic field can be estimated with:

$$B_{alt}(t) = D + A \cos(2\pi ft + \phi) \quad (31)$$

where  $B_{alt}$  is an alternating magnetic field,  $D$  is a DC component,  $A$  is the signal amplitude,  $f$  is a frequency of the signal (usually 50 or 60 Hz),  $\phi$  is its phase offset, and  $t$  is the time instance.

In our previous work [29], the method of extracting the amplitude and phase of the measured magnetometer signal is presented. The method is based on discrete Fourier transformation and has been shown to work at a frequency of 1 Hz and with a large number of samples. To increase the frequency of the system, an improved processing system based on numerical optimization is developed. This system is computationally more demanding but requires a smaller number of samples to determine  $A$ ,  $D$ , and  $\phi$ . The criterion used for optimization is [16]:

$$G_{alt}(A, D, \phi) = \sum_{i=1}^N (m_i - B_{alt}(i\delta_t))^2 \quad (32)$$

where  $m_i$  is the  $i$ th of  $N$  samples used for processing and  $\delta_t$  is the sampling time. The optimization is performed using the Nelder–Mead optimization algorithm, which is run twice for two different initial parameter sets ( $A_0, D_0, \phi_0$ ) for optimization (see Table 2).

**Table 2.** Initial parameters for optimization.

Parameter	Parameter Set 1	Parameter Set 2
$A_0$	$\sum_{i=1}^N \frac{m_i}{N}$	$\sum_{i=1}^N \frac{m_i}{N}$
$D_0$	$\max_i m_i - \min_i m_i$	$\max_i m_i - \min_i m_i$
$\phi_0$	$\phi_0^1$	$\phi_0^1 + \pi$

The same optimization procedure is repeated for all three magnetometers used for each of the  $x$ ,  $y$ , and  $z$  axes. If the phases of two axes coincide, they have the same direction, and if their phases are apart by  $\pi$  radians, they have the opposite direction. For this purpose, all measurements must be synchronized.

## 5. Experimental Results

This section describes the experiments conducted in the laboratory that were used to validate the localization and robot control methods presented.

### 5.1. Experimental Setup

Our experimental setup consisted of two parallel conductors approximately 3 m in length. An electric current of about 20 amperes flowed through each of the parallel conductors. To measure the magnetic field strength, we used three inertial measurement units (IMUs) attached to a special end effector with integrated magnetometers. The IMUs used were LMPS-CU2 and LPMS-RS2, which were equipped with a 3-axis magnetometer with a measurement range of 16 Gauss and a sampling rate of 200 Hz. The end effector also had two Dynamixel MX-64 <https://emanual.robotis.com/docs/en/dxl/mx/mx-64/> (accessed on 10 February 2023) as actuators to close the jaws of the electrical spacer and attach it to the power lines. Experiments were conducted on a PC using an Intel i7-10510U running at 1.8 GHz with 16 GB RAM and a GeForce MX330.

The control scheme shown in Figure 12 was implemented using the Schunk LWA4P robotic arm (see Figure 15) and the Controller Area Network (CAN) communication

protocol [34] with PCAN-USB <https://www.peak-system.com/PCAN-USB.199.0.html?L=1> (accessed on 10 February 2023).



**Figure 15.** Robot manipulator with end effector and power lines in background.

The achieved frequency of magnetic localization is about 10 Hz. The control frequency is 40 Hz, and it is limited by the current combination of software and hardware constraints. Possible control improvements in terms of smoother motion during servo control of the robot arm can be achieved with a higher control loop frequency defined by the message interval SYNC used for the synchronous cyclic position mode.

### 5.2. Experimental Results

The experiments were conducted using the parameters listed in Table 3.

Figure 16 shows the position of the end effector during the installation task, where the first 18 s is the motion during trajectory execution and from 18 to 32 s is the motion with robot arm servoing. The end effector position changes are smaller with servoing, which is a direct result of the gain configuration. In our experiments, we tested servoing with orientation constraints on the pitch and roll angles of the end effector and concluded that due to the lack of kinematic redundancy, we cannot avoid singularities that prevent the successful execution of the task. Therefore, we disabled servoing along the y-axis in the task space and took advantage of the fact that we can position the spacer anywhere along the global y-axis between the power lines.

**Table 3.** Experimental parameters used.

Parameter	Value	Parameter	Value
$K_{px}$	1.25	$d_{max}$	2 m
$K_{py}$	0	$I_{max}$	40 A
$K_{pz}$	1.25	$\Delta d$	0.1 m
$K_q$	1.0	$\Delta I$	2 A
$o$	0.2 m	$\delta d$	0.01 m
$a_{tl}$	0.15 m	$\delta I$	0.2 A
$\psi_o$	0.2 rad	N	20
$I_{cl}$	1.15 A	$t_1$	60 s
$t_2$	60 s	$t_3$	60 s
$d_1$	0.02	$d_2$	0.02

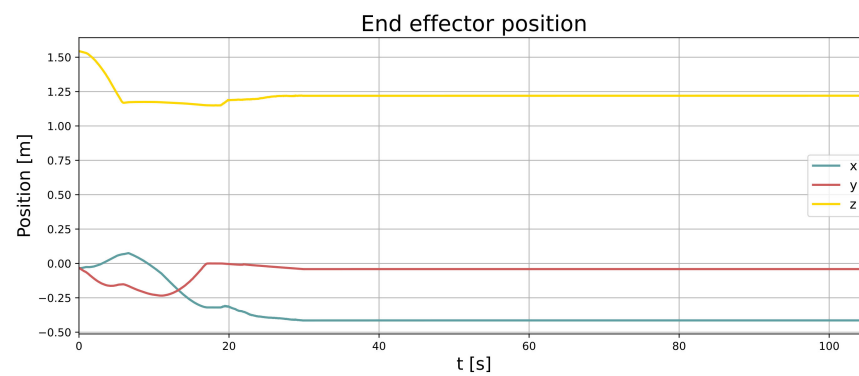
**Figure 16.** Position of the end effector during an installation procedure calculated with forward kinematics and joint position measurements.

Figure 17 shows the measurements of the first magnetometer, where we can see both measurement changes during arm movement and amplitude changes as we approach the power lines in the interval after 40 s.

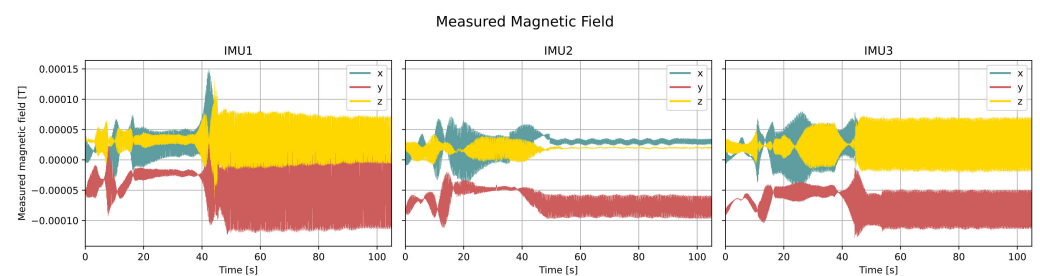
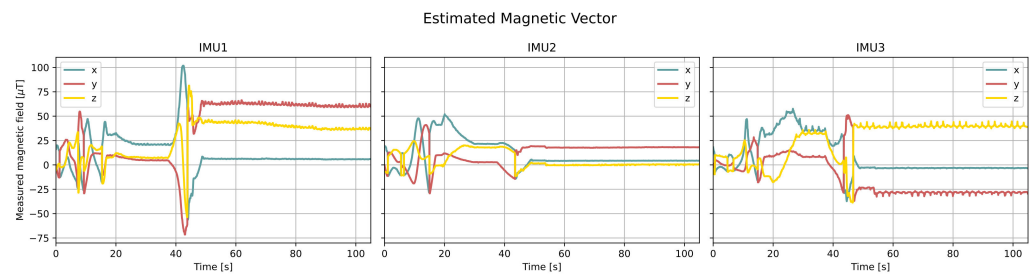
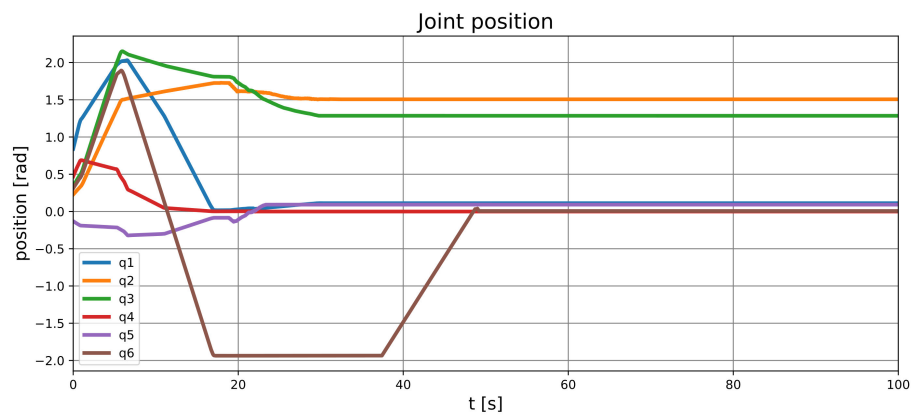
**Figure 17.** Magnetometer measurements during the installation procedure.

Figure 18 shows the magnetic field vector of the 50 Hz signal extracted from the magnetometer measurements during the installation of the spacer, and it can be seen how certain vector components change with the change in the end effector's position.



**Figure 18.** Estimated magnetic field vectors of the 50Hz signal extracted from each magnetometer during the installation task.

Figure 19 shows the joint positions during the installation task. The first 18 seconds show joint movement while executing the RRT planned trajectory based on  $x_{ap}$ . It is possible to see minor joint position changes when we use robotic servoing (18 s–30 s interval) to move the end effector to the installation pose.



**Figure 19.** Joint positions during the spacer installation procedure.

Figure 20 shows the position trajectory of the end effector during the installation task.

The trajectory in the  $x$ - $z$  plane and the  $y$ - $z$  plane of the global coordinate system is shown in Figure 21.

Figure 22 shows the right motor current during the installation task. We start tightening the bolts at 30 s and stop around 60 s when the current limit  $I_{cl}$  is reached with both motors for more than 20 s. The limit is the same for both motors.

Figure 23 shows the estimated installation position calculated based on the location of the power lines. At the start of the procedure, we use only one measurement to determine the  $x_{ap}$  pose. Because of that, minor changes in pose estimates in the first 18 s do not affect arm movements. A jump in the position estimate at 38 s can be attributed to the rotation of the end effector from  $x_{pp}$  to  $x_{ip}$ . It is possible to notice that during the robotic arm servoing (18–38 s), the estimation of the power line position stabilizes as the end effector approaches estimate  $x_{pp}$ .

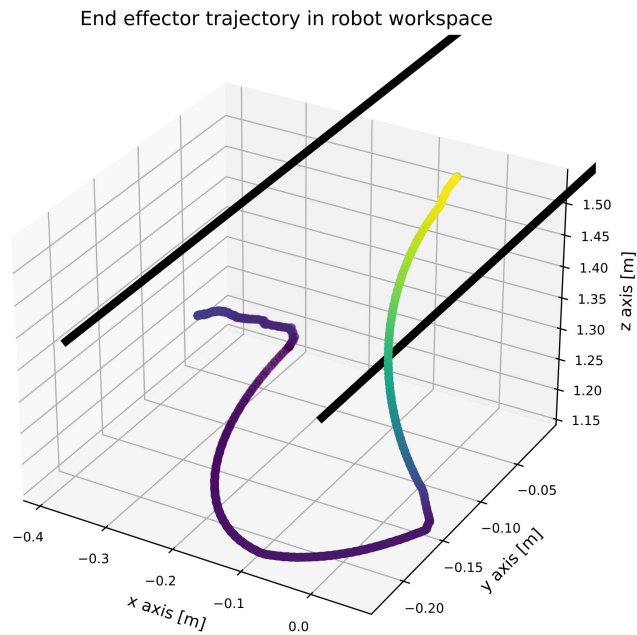


Figure 20. Executed trajectory during the spacer installation procedure.

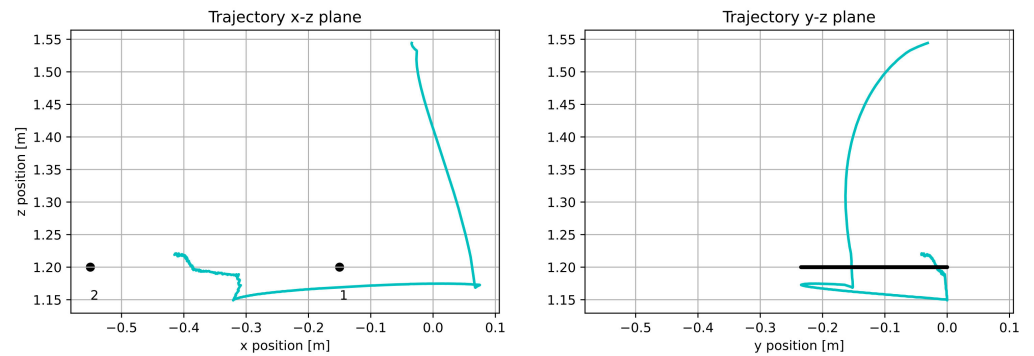


Figure 21. End effector position trajectory during the spacer installation procedure shown in  $x$ - $z$  plane and  $y$ - $z$  plane.

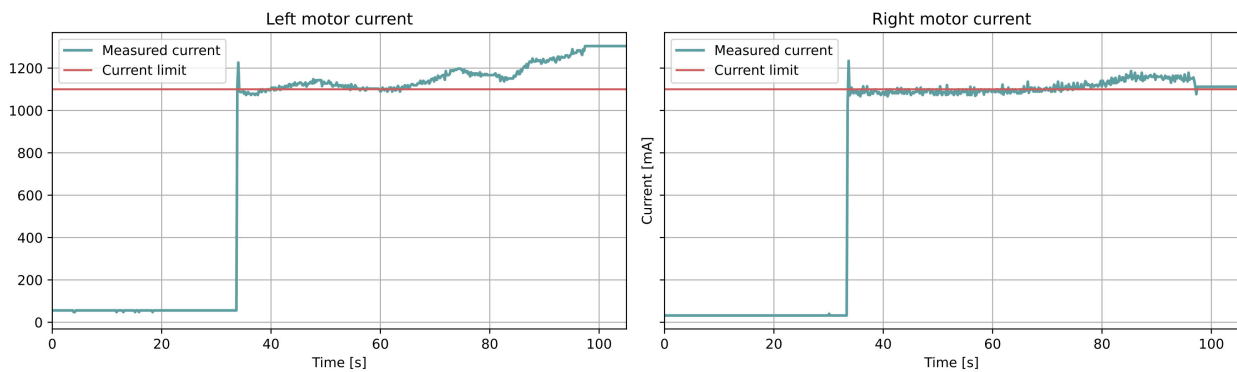
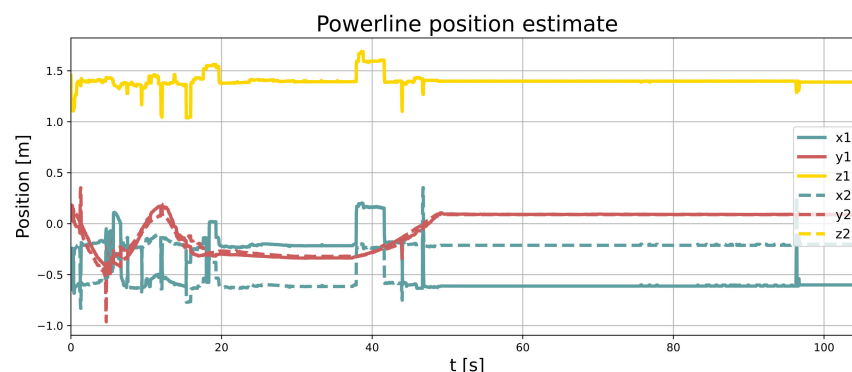


Figure 22. Motor currents during installation of spacer on conductors. We consider spacer closed if condition  $I_{mc} > I_{cl}$  is satisfied for more than 20 s.



**Figure 23.** Estimate of installation position calculated from the power line localization.  $x_1$ ,  $y_1$ , and  $z_1$  correspond to the estimated position of the power line closer to the robot arm base (1st line), whilst  $x_2$ ,  $y_2$ , and  $z_2$  correspond to the estimated position of the power line farther from the robot arm base (2nd line).

## 6. Discussion

In the Experiment section, we have experimentally demonstrated that it is possible to use a special end effector to install electrical spacers. We also identified some limitations that arise from the design of the end effector. These limitations include the need to precisely position the end effector (spacer with open jaws) between parallel power lines. The current design has only been tested when approaching the power line from below. We have shown that it is possible to install the spacer when locating power lines using magnetic localization and a conventional 6DOF robotic arm. The magnetic localization algorithm is limited to an operating frequency of 10 Hz, assuming parallel power lines with a predefined distance between them. Faster magnetic localization could be achieved by using other magnetometer sensors operating at a higher frequency. Another limitation imposed by the robotic arm used is the lack of kinematic redundancy.

## 7. Conclusions

We have presented a method for the autonomous installation of electrical spacers on power lines using a robotic manipulator with a specially designed end effector. The design of the end effector was presented, and the prototype was fabricated and tested. The prototype was used for the autonomous installation of spacers based on a localization system that relies on the measurement of the magnetic field generated by the current flow through the power lines. We have tested the methods under laboratory conditions, where the electrical spacer was successfully installed on the mock-up of two parallel current-carrying lines. The results show that magnetic localization combined with planned motion and servoing of the robotic manipulator enables the successful installation of electrical spacers on power lines.

Further work needs to be carried out to incorporate visual information and force control for spacer removal. There is also the possibility of incorporating damped least squares for singularity avoidance in the servo control of robotic manipulators. Such a system could be particularly useful for aerial manipulators that rely on visual information to estimate the location of power lines. The ultimate goal of the research described is to augment the aerial manipulator with a developed tooling and localization system that autonomously attaches electrical spacers to power lines, ensuring that this dangerous work does not have to be performed by humans.

**Supplementary Materials:** The following supporting information can be downloaded at: [https://github.com/larics/schunk\\_lwa4p\\_ros/tree/paper\\_v1](https://github.com/larics/schunk_lwa4p_ros/tree/paper_v1), code. A supporting video article is available at doi: <https://www.youtube.com/watch?v=BC1-fQ8PShE&feature=youtu.be>.



**Author Contributions:** Conceptualization, F.Z. and G.V.; methodology, F.Z. and G.V.; software, F.Z. and G.V.; end effector design, S.F.; visualization, G.V., F.Z. and S.F.; original draft preparation, F.Z. and G.V.; review, Z.K. and S.B.; supervision, Z.K.; funding acquisition, Z.K. and S.B. All authors have read and agreed to the published version of the manuscript.

**Funding:** This work was funded by the project AERIAL Cognitive Integrated Multi-task Robotic System with Extended Operation Range and Safety (AERIAL-CORE) EU-H2020-ICT (grant agreement No. 871479) and by the Croatian Science Foundation under the project “Young Researchers’ Career Development Project – Training New Doctoral Students” (DOK-2020-01).

**Data Availability Statement:** The data recorded during experiments were saved in bag format and are located at the following location: [https://github.com/larics/schunk\\_lwa4p\\_ros/tree/paper\\_v1/schunk\\_lwa4p\\_control/experiment\\_data](https://github.com/larics/schunk_lwa4p_ros/tree/paper_v1/schunk_lwa4p_control/experiment_data) (accessed on 10 February 2023).

**Conflicts of Interest:** The authors declare no conflict of interest.

### Abbreviations

The following abbreviations are used in this manuscript:

UAV	Unmanned Aerial Vehicle
AGV	Autonomous Guided Vehicle
MAGS	Magnetically Anchored and Guided System
CNN	Convolutional Neural Network
ROS	Robot Operating System
RRT	Rapid Random Trees
OMPL	Open Motion Planning Library
IMU	Inertial Measurement Unit
CAN	Controller Area Network
PLA	Polylactic acid

### References

1. INMR. Applying Interphase Spacers to Control Conductor Galloping. Available online: <https://www.inmr.com/applying-interphase-spacers-to-control-conductor-galloping/> (accessed on 22 October 2022).
2. Kim, H.S.; Nguyen, T.L. Analysis of galloping amplitude for conductors with interphase spacers. In Proceedings of the 30th Annual Conference of IEEE Industrial Electronics Society, IECON, Busan, Republic of Korea, 2–6 November 2004; Volume 2, pp. 1520–1525. [CrossRef]
3. Cacace, J.; Orozco-Soto, S.M.; Suarez, A.; Caballero, A.; Orsag, M.; Bogdan, S.; Vasiljevic, G.; Ebeid, E.; Rodriguez, J.A.A.; Ollero, A. Safe Local Aerial Manipulation for the Installation of Devices on Power Lines: AERIAL-CORE First Year Results and Designs. *Appl. Sci.* **2021**, *11*, 6220. [CrossRef]
4. 516-1995; IEEE Guide for Maintenance Methods on Energized Power Lines. IEEE: New York, NY, USA, 2009; pp. 1–144. [CrossRef]
5. Ollero, A.; Tognon, M.; Suarez, A.; Lee, D.; Franchi, A. Past, Present, and Future of Aerial Robotic Manipulators. *IEEE Trans. Robot.* **2022**, *38*, 626–645. [CrossRef]
6. Pouliot, N.; Montambault, S. Geometric design of the LineScout, a teleoperated robot for power line inspection and maintenance. In Proceedings of the IEEE International Conference on Robotics and Automation, Pasadena, CA, USA, 9–23 May 2008; pp. 3970–3977. [CrossRef]
7. Miller, R.; Abbasi, F.; Mohammadpour, J. Power Line Robotic Device for Overhead Line Inspection and Maintenance. *Ind. Robot.* **2017**, *44*, 75–84. [CrossRef]
8. Yang, D.; Feng, Z.; Ren, X.; Lu, N. A novel power line inspection robot with dual-parallelogram architecture and its vibration suppression control. *Adv. Robot.* **2014**, *28*, 807–819. [CrossRef]
9. Yu, F.; Kai, W.; Shaolei, W. Design of clamping device for overhead line branch line with live installation. In Proceedings of the International Conference on Artificial Intelligence and Electromechanical Automation, AIEA, Tianjin, China, 26–28 June 2020; pp. 321–324. [CrossRef]
10. Jayatilaka, M.; Shamugavel, M.; Ragavan, S.V. Robonwire: Design and development of a power line inspection robot. In Proceedings of the 1st International and 16th National Conference on Machines and Mechanisms, iNaCoMM, Roorkee, India, 18–20 December 2013.
11. Stuhne, D.; Hoang, V.D.; Vasiljevic, G.; Bogdan, S.; Kovacic, Z.; Ollero, A.; Ebeid, E.S.M. Design of a Wireless Drone Recharging Station and a Special Robot End Effector for Installation on a Power Line. *IEEE Access* **2022**, *10*, 88719–88737. [CrossRef]
12. Campos, M.F.; Pereira, G.A.; Vale, S.R.; Bracarense, A.Q.; Pinheiro, G.A.; Oliveira, M.P. A mobile manipulator for installation and removal of aircraft warning spheres on aerial power transmission lines. In Proceedings of the IEEE International Conference on Robotics and Automation, Washington, DC, USA, 11–15 May 2002; Volume 4, pp. 3559–3564. [CrossRef]

13. Ruaux, P. Mechanisation of the installation of aircraft warning spheres on overhead lines. In Proceedings of the IEEE 7th International Conference on Transmission and Distribution Construction, Operation and Live-Line Maintenance ESMO, Columbus, OH, USA, 29 October–3 November 1995; pp. 125–131. [\[CrossRef\]](#)
14. Moore, J.; Tedrake, R. Magnetic localization for perching UAVs on powerlines. In Proceedings of the 2011 IEEE/RSJ International Conference on Intelligent Robots and Systems, San Francisco, CA, USA, 25–30 September 2011; pp. 2700–2707. [\[CrossRef\]](#)
15. Martinović, D.; Bogdan, S.; Kovačić, Z. Mathematical Considerations for Unmanned Aerial Vehicle Navigation in the Magnetic Field of Two Parallel Transmission Lines. *Appl. Sci.* **2021**, *11*, 3323. [\[CrossRef\]](#)
16. Vasiljevic, G.; Martinovic, D.; Batos, M.; Bogdan, S. Validation of two-wire power line UAV localization based on the magnetic field strength. In Proceedings of the International Conference on Unmanned Aircraft Systems, ICUAS, Dubrovnik, Croatia, 21–24 June 2022; pp. 434–441. [\[CrossRef\]](#)
17. Lee, N.; Ahn, S.; Han, D. AMID: Accurate Magnetic Indoor Localization Using Deep Learning. *Sensors* **2018**, *18*, 1598. [\[CrossRef\]](#) [\[PubMed\]](#)
18. Lu, C.X.; Li, Y.; Zhao, P.; Chen, C.; Xie, L.; Wen, H.; Tan, R.; Trigoni, N. Simultaneous Localization and Mapping with Power Network Electromagnetic Field. In Proceedings of the 24th Annual International Conference on Mobile Computing and Networking MobiCom, New Delhi, India, 29 October–2 November 2018; pp. 607–622. [\[CrossRef\]](#)
19. Gietler, H.; Ammari, H.; Zangl, H. Robust Electromagnetic Pose Estimation for Robotic Applications. *IEEE Trans. Instr. Measur.* **2020**, *69*, 4258–4269. [\[CrossRef\]](#)
20. He, X.; Zheng, H.C. Magnetic localization and orientation of the capsule endoscope based on a random complex algorithm. *Med. Dev.* **2015**, *8*, 175–184. [\[CrossRef\]](#)
21. Kamewaka, S.; Uemura, S. A magnetic guidance method for automated guided vehicles. *IEEE Trans. Mag.* **1987**, *23*, 2416–2418. [\[CrossRef\]](#)
22. Siciliano, B.; Khatib, O. *Springer Handbook of Robotics*; Springer: Berlin/Heidelberg, Germany, 2007. [\[CrossRef\]](#)
23. Park, S.Y.; Kim, Y.J.; Lee, J.J.; Kim, B.S.; Alsaif, K.A. Controlling robot arm manipulator using image-based visual servoing without pre-depth information. In Proceedings of the 37th Annual Conference of the IEEE Industrial Electronics Society IECON, Melbourne, VIC, Australia, 7–10 November 2011; pp. 3276–3280. [\[CrossRef\]](#)
24. Gong, Z.; Tao, B.; Yang, H.; Yin, Z.; Ding, H. An Uncalibrated Visual Servo Method Based on Projective Homography. *IEEE Trans. Autom. Sci. Eng.* **2018**, *15*, 806–817. [\[CrossRef\]](#)
25. Tsai, M.C.; Yang, C.H. A Flux-Density-Based Electromagnetic Servo System for Real-Time Magnetic Servoing/Tracking. *IEEE/ASME Trans. Mech.* **2008**, *13*, 249–256. [\[CrossRef\]](#)
26. Li, W.; Cheng, T.; Ye, M.; Ng, C.S.H.; Chiu, P.W.Y.; Li, Z. Kinematic Modeling and Visual Servo Control of a Soft-Bodied Magnetic Anchored and Guided Endoscope. *IEEE/ASME Trans. Mech.* **2020**, *25*, 1531–1542. [\[CrossRef\]](#)
27. Ribeiro, E.G.; de Queiroz Mendes, R.; Grassi, V. Real-time deep learning approach to visual servo control and grasp detection for autonomous robotic manipulation. *Rob. Auton. Syst.* **2021**, *139*, 103757. [\[CrossRef\]](#)
28. Curtis, B. Robotic Arm Calibration and Control 6-DOF Powerball LWA 4. Available online: [https://foswiki.cs.rpi.edu/foswiki/pub/RoboticsWeb/LabPublications/bradley\\_ROBOTIC\\_ARM\\_CALIBRATION\\_CTRL\\_report.pdf](https://foswiki.cs.rpi.edu/foswiki/pub/RoboticsWeb/LabPublications/bradley_ROBOTIC_ARM_CALIBRATION_CTRL_report.pdf) (accessed on 10 April 2023).
29. Vasiljević, G.; Martinović, D.; Orsag, M.; Bogdan, S. Grabbing power line conductors based on the measurements of the magnetic field strength. In Proceedings of the Aerial Robotic Systems Physically Interacting with the Environment (AIRPHARO), Biograd na Moru, Croatia, 4–5 October 2021; pp. 1–7. [\[CrossRef\]](#)
30. Zelenak, A.; Reid, R.; Pettinger, A.; Pryor, M. Reactive Motion Control for Real-Time Teleoperation and Semi-Autonomous Contact Tasks. In Proceedings of the 2019 IEEE/RSJ International Conference on Intelligent Robots and Systems (IROS 2019), Macau, China, 3–8 November 2019. [\[CrossRef\]](#)
31. Şucan, I.A.; Moll, M.; Kavraki, L.E. The Open Motion Planning Library. *IEEE Rob. Autom. Mag.* **2012**, *19*, 72–82. [\[CrossRef\]](#)
32. Yuan, J. Closed-loop manipulator control using quaternion feedback. *IEEE J. Rob. Autom.* **1988**, *4*, 434–440. [\[CrossRef\]](#)
33. Harel, D. Statecharts: a Visual Formalism for Complex Systems. *Sci. Comp. Program.* **1987**, *8*, 231–274. [\[CrossRef\]](#)
34. Chen, H.; Tian, J. Research on the Controller Area Network. In Proceedings of the International Conference on Networking and Digital Society, Guiyang, China, 30–31 May 2009; Volume 2, pp. 251–254. [\[CrossRef\]](#)

**Disclaimer/Publisher’s Note:** The statements, opinions and data contained in all publications are solely those of the individual author(s) and contributor(s) and not of MDPI and/or the editor(s). MDPI and/or the editor(s) disclaim responsibility for any injury to people or property resulting from any ideas, methods, instructions or products referred to in the content.